JOURNAL OF GEOPHYSICAL RESEARCH, VOL. 105, NO. D4, PAGES 4607–4624, FEBRUARY 27, 2000

Impact of global warming on the Asian winter monsoon in a coupled GCM

Zeng-Zhen Hu, [1] Lennart Bengtsson, and Klaus Arpe

Max-Planck-Institut für Meteorologie, Hamburg, Germany

Abstract. The Asian winter monsoon (AWM) response to the global warming was investigated through a long-term integration of the transient greenhouse warming with the ECHAM4/OPYC3 CGCM. The physics of the response was studied through analyses of the impact of the global warming on the variations of the ocean and land contrast near the ground in the Asian and western Pacific region and the east Asian trough and jet stream in the middle and upper troposphere. Forcing of transient eddy activity on the zonal circulation over the Asian and western Pacific region was also analyzed. It is found that in the global warming scenario the winter northeasterlies along the Pacific coast of the Eurasian continent weaken systematically and significantly, and intensity of the AWM reduces evidently, but the AWM variances on the interannual and interdecadal scales are not affected much by the global warming. It is suggested that the global warming makes the climate over the most part of Asia to be milder with enhanced moisture in winter. In the global warming scenario the contrasts of the sea level pressure and the near-surface temperature between the Asian continent and the Pacific Ocean become significantly smaller, northward and eastward shifts and weakening of the east Asian trough and jet stream in the middle and upper troposphere are found. As a consequence, the cold air in the AWM originating from the east Asian trough and high latitudes is less powerful. In addition, feedback of the transient activity also makes a considerable contribution to the higher-latitude shift of the jet stream over the North Pacific in the global warming scenario.

1. Introduction

Climate variability in Asia is an integral component of the global climate system. Summer climate variabilities in Asia are closely related with the variations of Asian summer monsoon system and have been extensively studied both in model simulations and in data analyses by many investigators [*WCRP*, 1998]. The active role of the Asian summer monsoon on the intraseasonal and interannual timescale variations of the global climate system has been suggested [*Yasunari*, 1991; *Lau*, 1992]. However, the research on the Asian winter monsoon (AWM) is relatively limited. The most prominent surface feature of the AWM is the strong northeasterly flow (NE) along the eastern flank of the Siberian high and the east coast of the Eurasian continent. The strong NE, starting from the front edge of the Siberian high, periodically pushes toward lower latitudes to become a winter monsoon surge [*Ji et al.*, 1997]. The NE dominates a vast area of the tropical and extratropical regions of Asia and the western Pacific for nearly half a year [*Ding*, 1991; *Chen et al.*, 1991]. The AWM variation is closely related with the land-ocean contrast near the ground, and the locations and intensities of the east Asian trough and jet stream in the middle and upper troposphere, and cohered with variation of the Hadley cell over the Asian and western Pacific region [*Ding*, 1991; *Chen et al.*, 1991]. The AWM is one of the most active and powerful circulation in the Northern Hemisphere (NH) winter. It is believed that the AWM is one of the most important medium to the interaction between tropics and extratropics and between the two hemispheres.

Anomalies of the AWM do not only bring anomalous weather and climate (cold or warm winter) in Asia [*Ding*, 1991; *Chen et al.*, 1991] but also link to the variations of large-scale general circulation [*Ding*, 1991; *Chen and Graf*, 1999], tropical convection and tropospheric circulation [*Compo et al.*, 1999], convective activity over the tropical maritime continents [*Chang et al.*, 1979] and the western Pacific [*Hu and Nitta*, 1997], and the air-sea interaction in the tropical central and eastern Pacific [*Li et al.*, 1988; *Ji et al.*, 1997]. *Sun*

[1] Also at Institute of Atmospheric Physics, Chinese Academy of Sciences, Beijing.

Paper number 1999JD901031.
0148-0227/00/1999JD901031$09.00

and Sun [1994] have found that the AWM anomaly is a precursor to the following summer drought and flood in China. The impacts of the AWM variations on the air-sea coupling in the tropical Pacific, the following summer drought and flood in China and the Asian summer monsoon are mainly through the memory of sea surface temperature (SST), snow cover, and soil moisture over the Eurasian continent. It seems that the AWM plays an important and active role in the global atmosphere-ocean-land interaction system. Therefore a study on the variability of the AWM is not only important to recognize the role of the AWM in this region but also beneficial for a better understanding of the variability of the global atmosphere-ocean-land system.

Investigations of climate changes in China during the last 44 years [*Nitta and Hu*, 1996] and the last 100 years [*Wang and Ye*, 1993] have shown a pronounced warming trend in North China and a minor cooling trend in the central part of China. With observational data and model simulations of the climate change in the east Asian region, *Hulme et al.* [1994] also indicated the possible impact of the global warming on variations of temperature and precipitation for the east Asian region. It seems that the global warming will have significant impacts on the climate in Asia [*Hulme et al.*, 1994]. Investigating the response of the AWM to the transient greenhouse gas concentration changes will help understanding the present climate variation and predicting the future change due to the anthropogenic effect, not only in Asia but also globally.

In this work the AWM response to the global warming and the physical mechanisms are investigated on the basis of a long-term integration with a time-dependent greenhouse gas concentration increase in a coupled atmosphere-ocean-sea ice-land surface model. In section 2 the coupled model, experiments, and data are briefly described. Simulated AWM variations, including wind field at 10 m, total precipitation, and surface evaporation, in response to the greenhouse warming, are analyzed in section 3. The involved mechanism is investigated in section 4 through analyzing the variations of the land-ocean contrast near the ground, the east Asian trough and jet stream in the middle and upper troposphere, and the transient feedback on the zonal circulation in the Asian and Pacific region. Section 5 contains a summary and discussion.

2. Model, Experiment, and Data

2.1. Model

The climate model is a global coupled atmosphere-ocean-sea ice-land surface climate model, the ECHAM4/OPYC3 CGCM. The atmospheric and land surface components of the CGCM are the ECHAM4, which is a spectral model of triangular truncation with total horizontal wavenumber 42 (T42) and with 19 vertical levels. The ECHAM4 includes a comprehensive set of physical parameterizations, such as radiation, vertical diffusion, gravity wave drag, cumulus convection, shallow convection, stratiform clouds, and a simple model for soil processes. The soil model comprises the budgets of heat and water in the soil, the snow pack over land, and the heat budget of land ice. Prognostic variables are vorticity, divergence, surface pressure, temperature, water vapor, and cloud water. The ECHAM4 model has been tested extensively and has been found to reproduce the present atmospheric circulation with a high level of realism [*e.g., Roeckner et al.*, 1996b; *Chen and Roeckner*, 1996]. A detailed description of the ECHAM4 model is given by *Roeckner et al.* [1996a, and references therein].

The OGCM component is an updated version (OPYC3) of the OPYC oceanic general circulation model developed by *Oberhuber* [1993a, b]. The OPYC3 uses isopycnals as the vertical coordinate system of the oceanic GCM. The OPYC3 consists of three submodels; the interior ocean, the surface mixed layer, and the sea ice, respectively. The OPYC3 includes a realistic equation of state, employs primitive equations, and has a surface mixed layer coupled to a snow and sea ice model. A surface mixed layer is coupled also to the interior ocean in order to represent near-surface vertical mixing and to improve the response timescales to atmospheric forcing which is controlled by the mixed layer thickness of the ocean. Poleward of 36°, the horizontal resolution is identical to the Gaussian grid of the atmospheric model (2.8125° for the T42 model). In low latitudes the meridional spacing is gradually decreased to 0.5° at the equator. In the vertical, 10 interior layers below the surface mixed layer are used. The sea ice model calculates the thickness and concentration of ice and its momentum. A detailed description of the OPYC3 model can be found in the work of *Oberhuber* [1993a, b].

The ECHAM4 and OPYC3 are coupled through a mutual exchange of fluxes. Fluxes of momentum are unconstrained, while fluxes of heat and fresh water are flux adjusted but only as annual averages. The ECHAM4 is driven with SSTs simulated by the OPYC3, and the OPYC3 is forced by the momentum, heat, and freshwater fluxes given by the ECHAM4. The ECHAM4/OPYC3 CGCM has also been thoroughly evaluated in extensive control integrations [*Roeckner et al.*, 1996a; *Bacher et al.*, 1998] and a global warming run [*Hu et al.*, 1999; *Bengtsson*, 1997, 1996]. It has been demonstrated that the ECHAM4/OPYC3 CGCM can reasonablely simulate the present climate, its variability and future climate change in the global warming scenario. The detailed coupling strategy and technology of the ECHAM4 and OPYC3 are described by *Bengtsson* [1996] and *Bacher et al.* [1998].

2.2. Experiment and Data

The experiment is a 240 year long simulation of the transient greenhouse gas warming (GHG). In the GHG run, from 1860 to 1990, the annual concentrations of the greenhouse gases are prescribed as observed and,

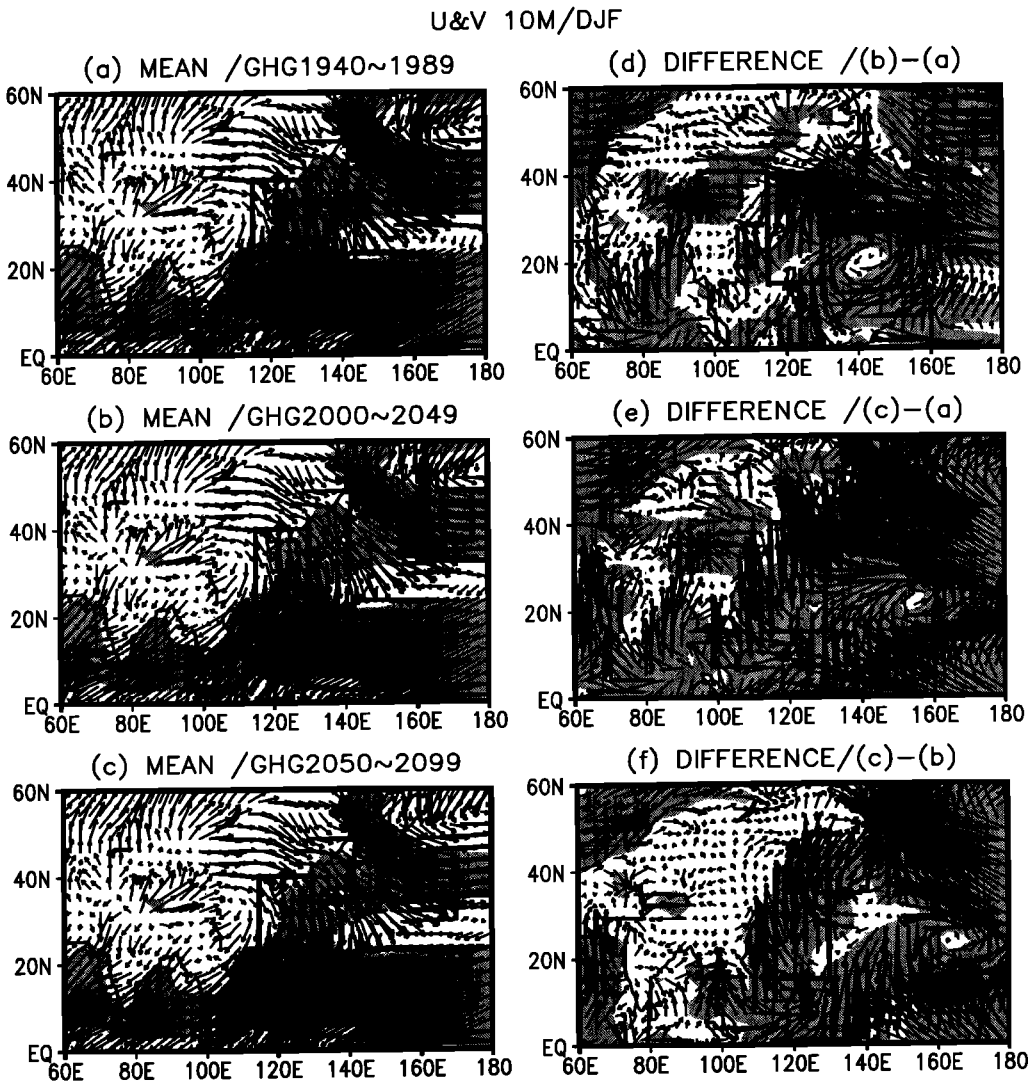

Figure 1. Mean wind fields at 10 m in winter (DJF) averaged for (a) the GHG 1940 ~ 1989, (b) the GHG 2000 ~ 2049, and (c) the GHG 2050 ~ 2099, and their differences: (d) Figures 1b minus 1a, (e) Figures 1c minus 1a, and (f) Figures 1c minus 1b. The rectangular frames indicate the area where the Asian winter monsoon index (AWMI) is averaged. Shading marks the regions with values of wind speed greater than 4 m/s in Figures 1a-1c, and 0.2 m/s in Figures 1d-1f.

from 1990 onward, according to IPCC scenario IS92a [*Intergovernmental Panel on Climate Change (IPCC)*, 1992]. The transient integration starts in the year 1860 and ends in the year 2099 (denoted by GHG 1860 ~ 2099). More details on the GHG experiment can be found in the work of *Roeckner et al.* [1999]. *Bengtsson* [1997, 1996] compared the El Niño-Southern Oscillation (ENSO) cycle, low-frequency variability, feedback processes, energy cycle, and hydrological cycle of this long-term integration with that in a corresponding control run. With the GHG run, *Hu et al.* [1999] investigated the impact of the global warming on the trend and standard deviation of geopotential height at 500 hPa in winter, on the variabilities of the large-scale interannual and interdecadal climate modes, and on the ENSO cycle and the teleconnection patterns. In the present work we focus on the AWM climate varying with the greenhouse gas concentrations and the involved mechanism in the GHG run.

The data used include seasonal means of temperature at 2 m (T2m), geopotential height difference between 300 hPa and 700 hPa (H300 − H700), wind field (u and v) at 10 m and 300 hPa, and the sea level pressure (SLP) in December, January, and February (DJF) in the GHG run. Divergences at 200 hPa in DJF are also used to examine the variations of the Hadley cell over the Asian and western Pacific region due to the greenhouse gas concentration changes in the GHG run. The investigation is focused on the comparison of the present climate of the model (represented by the GHG 1940 ~ 1989) with simulation of future climate in two different periods with significant warming (represented

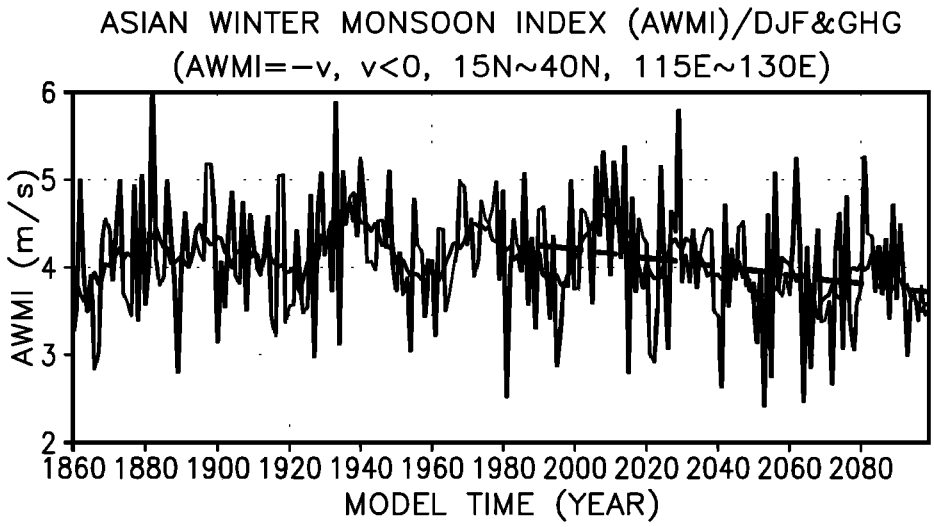

Figure 2. Variations of the AWMI in the GHG 1860 ~ 2099. The smoothed line represents the 9-year running mean. The long-dashed line is the linear trend of the AWMI during the GHG 1990 ~ 2099, which is different from zero at the significance level of 98% using the T test. The unit of the AWMI is m/s. The linear trend of the AWMI is −0.005 m/s per year for the period of the GHG 1990 ~ 2099.

by the GHG 2000 ~ 2049 and GHG 2050 ~ 2099). In addition, with a 2-6 day bandpass filter data, seasonal (DJF) means of the zonal component of the localized Eliassen − Palm flux at 300 hPa,

$$E = [(\overline{v'^2} - \overline{u'^2})/2, -\overline{u'v'}],$$

and its divergence ($\nabla \bullet E$) are calculated on the basis of the definition given by *Trenberth* [1986], where u' and v' are the transient components of daily data with the 2-6 day bandpass filter, and $\overline{u'^2}$, $\overline{v'^2}$, and $\overline{u'v'}$ represent the seasonal mean. Only the decadal (10 years) averages (GHG 1980 ~ 1989, GHG 2030 ~ 2039, GHG 2070 ~ 2079, and GHG 2090 ~ 2099) of the localized Eliassen-Palm flux and their divergence and the differences in winter (DJF) are used to identify the role of the transient eddy activity on the variation of the AWM general circulation in the global warming scenario.

3. Simulated AWM Variations

The impact of global warming on the AWM is revealed in this section through analyzing the variations of the wind fields at 10 m, total (large-scale and convective) precipitation, surface evaporation, and the differences between the total precipitation and the evaporation in different periods of the model simulations. Evolution of an AWM index (AWMI) is examine for its linear trend and variances on the interannual and interdecadal scales.

3.1. Wind Fields at 10 m

The wind fields at 10 m over the Asian and western Pacific regions in DJF averaged for the (Figure 1a) GHG 1940 ~ 1989, (Figure 1b) 2000 ~ 2049 and (Figure 1c) GHG 2050 ~ 2099 and their difference (Figures 1d, 1e, and 1f) are shown in Figure 1. Figure 1 demonstrates that the AWM is strongly related to the surface cold high over Siberia (Siberian anticyclone). In addition, Figure 1 suggests some associations between the AWM and the general circulation over the Pacific Ocean and India Ocean. In comparisons of the simulations (Figures 1a, 1b, and 1c) with observations [*Chen et al.*, 1991; *Ding*, 1991; *Chen and Graf*, 1999] it is indicated that the spatial distribution pattern of the AWM with strong northerlies along the Pacific coast of the Eurasian continent is quite well simulated by the ECHAM4/OPYC3 CGCM. Thus it is reasonable to investigate the AWM response to the global warming and the involved mechanism with the CGCM.

The impact of the global warming on the AWM is demonstrated in Figures 1d, 1e, and 1f. In comparison with the present climate (GHG 1940 ~ 1989) (Figure 1a) the northerlies are weakened in the global warming scenario (GHG 2000 ~ 2049 and GHG 2050 ~ 2099) (Figures 1b, 1c), and the anomalous southerlies are dominating Figures 1d, 1e, and 1f along the coast regions from the Indian peninsula to Japan via the Indochina peninsula and China. The impact is more pronounced in the GHG 2050 ~ 2099 than in the GHG 2000 ~ 2049 (Figures 1d, 1e, and 1f). Figure 2 shows the interannual evolution of the AWMI in the GHG 1860 ~ 2099. The AWMI is defined as the average of $-v$ with $v < 0$ over the region of 15°N ~ 40°N, 115°E ~ 130°E (see the rectangles in Figure 1), and v is the seasonal mean of the meridional wind at 10 m. This definition is similar to that given by *Ji et al.* [1997] and *Chen and Graf* [1999]. Large interannual and interdecadal variations of the AWMI are evident in Figure 2. The linear

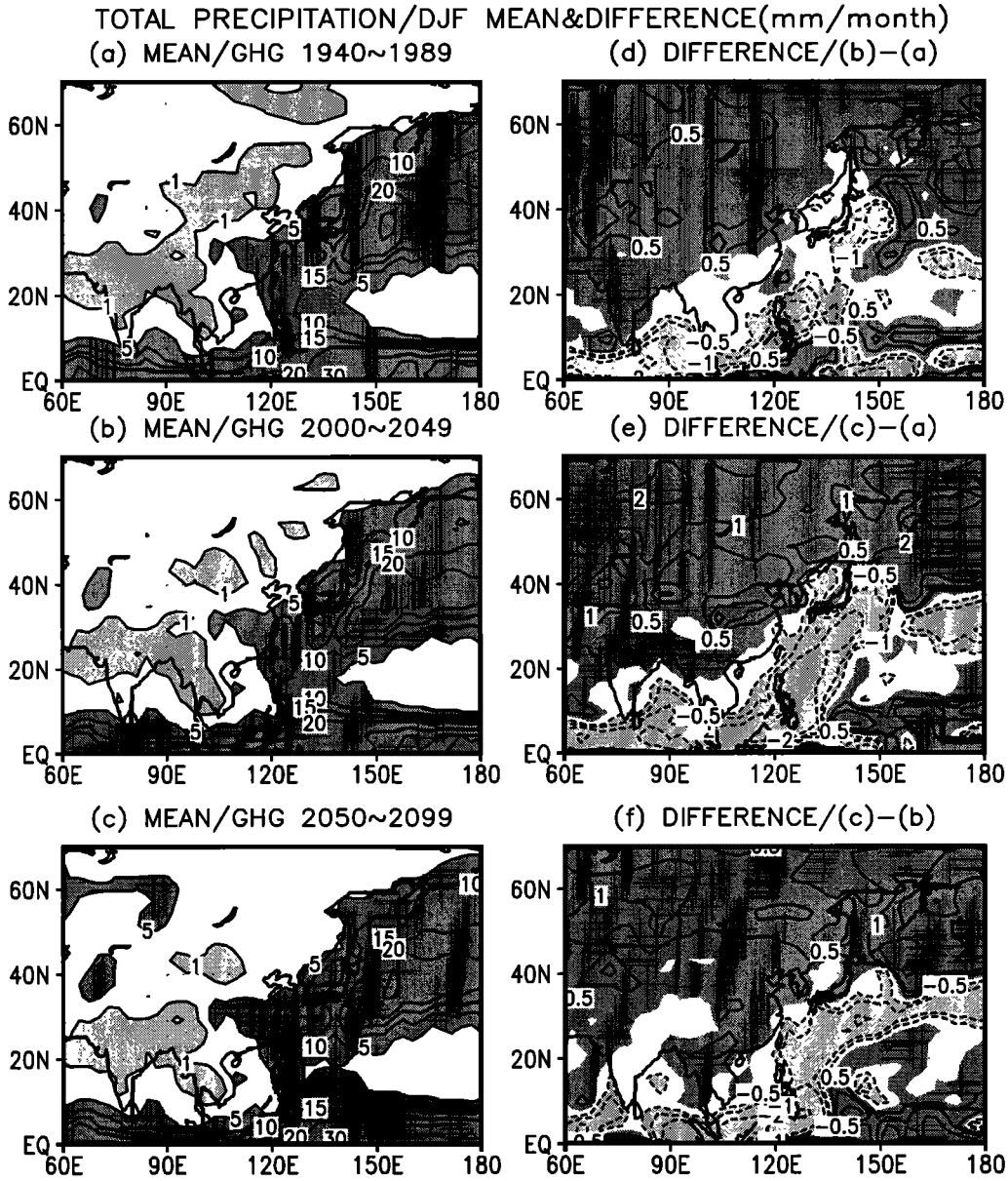

Figure 3. Average of the total precipitation in (a) the GHG 1940 ~ 1989, (b) the GHG 2000 ~ 2049, (c) the GHG 2050 ~ 2099, and their differences: (d) Figures 3b minus 3a, (e) Figures 3c minus 3a, and (f) Figures 3c minus 3b. Contours are at 1, 5, 10, 15, 20, 30, 40, and 50 mm/month in Figures 3a-3c, at −5, −2, −1, −0.5, 0.5, 1, 2 mm/month in Figures 3d-3f. Darker (lighter) shading indicates the regions with values greater (less) than 5 (1) mm/month in Figures 3a-3c, 0.0 (−0.5) mm/month in Figures 3d-3f.

decreasing trend of the AWMI is pronounced after the year 1990, which is different from zero at the significance level of 98% using the T test. The linear trend in Figure 2 is consistent with the difference shown in Figures 1d, 1e, and 1f. Therefore the intensity of the AWM will be reduced systematically and significantly in the global warming scenario. Variances of the detrended AWMI are, however, similar in the different period of the GHG run. It means that the interannual and interdecadal variances of the AWM are not affected much by the global warming.

3.2. Total Precipitation and Surface Evaporation

The distribution patterns of total precipitation are similar for the various periods of the GHG run with large values in the tropics and the northwestern and western Pacific and small values over the Asian continent (Figures 3a, 3b, and 3c), but their amounts change considerably in the temperate and high latitudes of Asia and the Indian Ocean and the western Pacific region (Figures 3d, 3e, and 3f). The total precipitation will

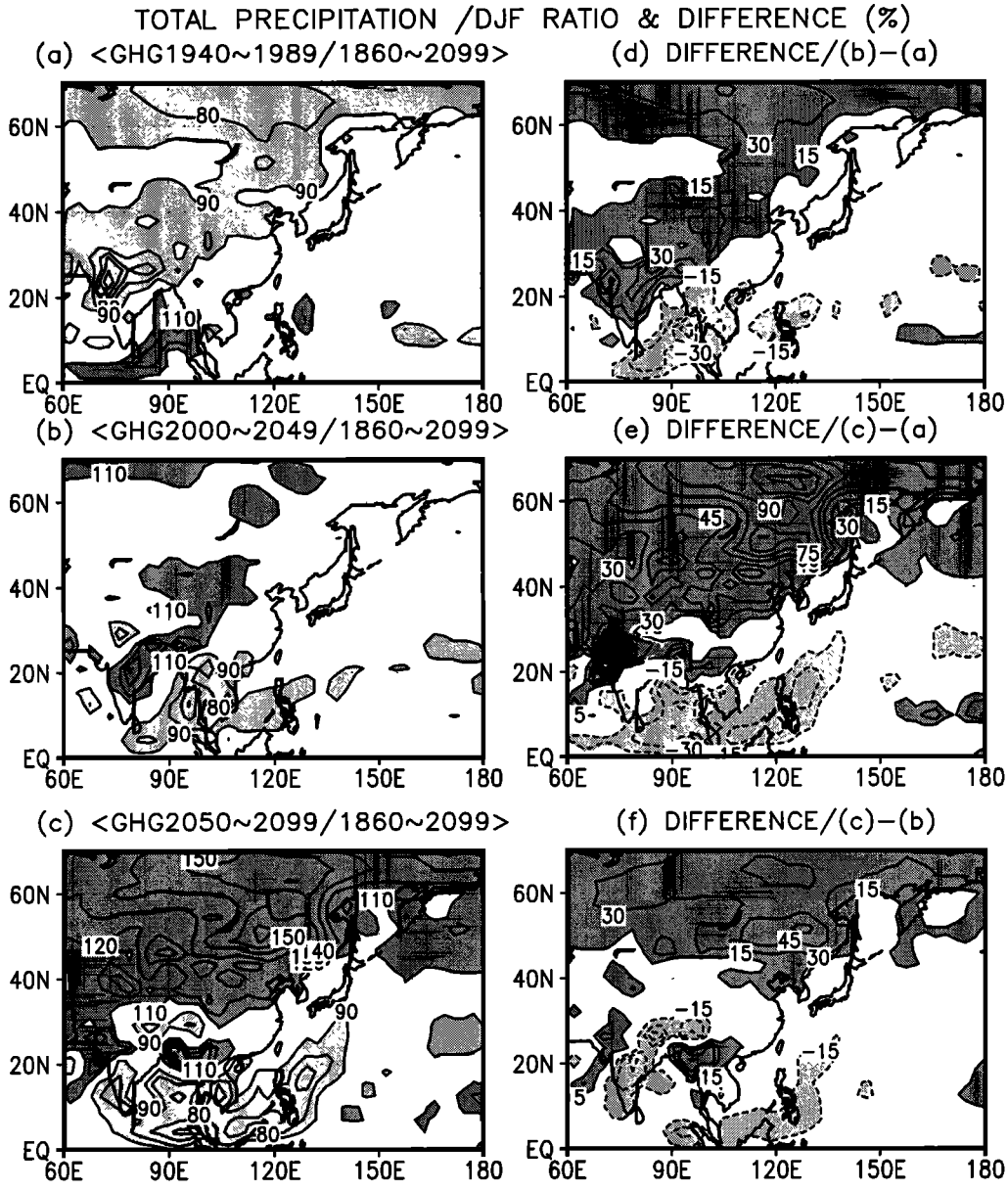

Figure 4. Same as Figure 3 but for the ratios of the total precipitation in different periods to that in the whole integration (GHG 1860 ~ 2099). Contour intervals are 10% in Figures 4a-4c, and 15% in Figures 4d-4f. Contours with values of 100% in Figures 4a-4c, and 0% in Figures 4d-4f are omitted. Darker (lighter) shading indicates the regions with values greater (less) than 110% (90%) in Figures 4a-4c, and 15% (−15%) in Figures 4d-4f.

increase over the North Pacific, the tropical central Pacific, and the most parts of the Asian continent, especially in the temperate and high latitudes of the continent (Figures 3d, 3e, and 3f). The increase of the precipitation in the northern and central parts of Asia in the global warming scenario takes place mainly as solid (snowfall) and liquid precipitation (figures are not shown), respectively. It seems that the area and thickness of the snow cover in the northern part of Asia will increase in the global warming scenario.

Since the amounts of the total precipitation is small in the northern part of Asia, the total precipitation changes are more clearly demonstrated through comparison of the ratios of the total precipitation (Figure 4). In the GHG 2050 ~ 2099 the total precipitation will increase by more than 15% in the northern part of Asia and decrease more than 15% in the regions from the Indian Ocean to the southwestern Pacific (Figure 4e). It is noted that the precipitation change is not pronounced in the regions from Indochina peninsula to Japan via the western Pacific and the southeastern part of China (Figures 3d, 3e, 3f, 4d, 4e, and 4f). This is also coherent with the regional average of the total precipitation in the southern Asia and Tibetan Plateau shown in Figures 5b and 5c. The precipitation increasing (decreasing) is coherent with the convergence (divergence)

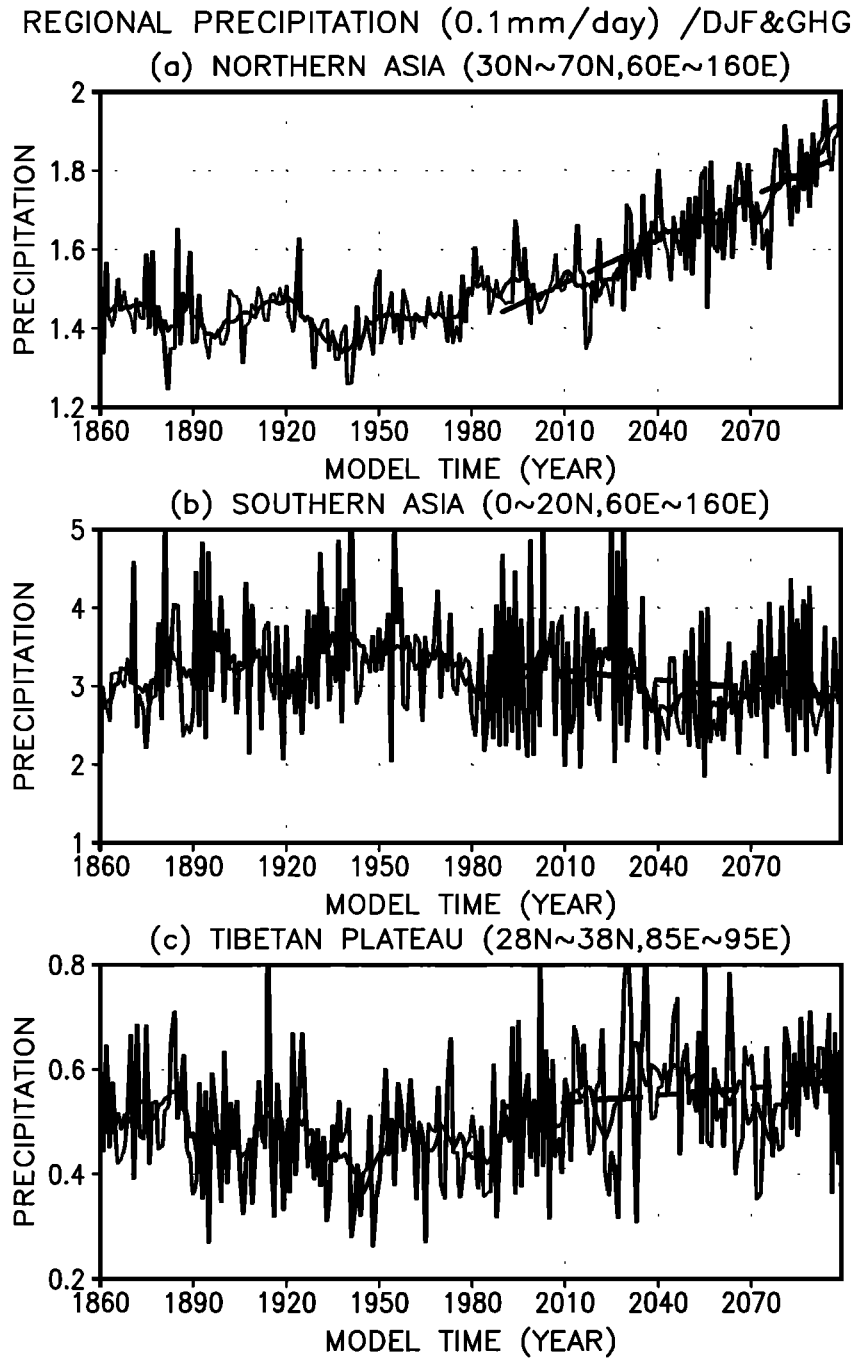

Figure 5. Average of the total precipitation in (a) northern Asia (30°N ~ 70°N, 60°E ~ 160°E), (b) southern Asia (0° ~ 20°N, 60°E ~ 160°E), and (c) over the Tibetan Plateau (28°N ~ 38°N, 85°E ~ 95°E). The units are 0.1 mm/d. The smoothed lines and long-dashed lines represent the 9 year running mean and the linear trends during the GHG 1990 ~ 2099. The linear trends are 0.00036, −0.00039 and 0.00005 mm/d per year for the period of the GHG 1990 ~ 2099 in Figures 5a-5c, respectively. The linear trend in Figure 5a is different from zero at the significance level of 99% using the T test.

of the wind field changes as shown in Figures 1d, 1e, and 1f. The increase of the precipitation over Asia is more pronounced in the high latitudes than in the low latitudes of Asia and in the GHG 2050 ~ 2099 than in the GHG 2000 ~ 2049 (Figures 4d, 4e, and 4f).

Analyses of the regional average of the total precipitation show that the precipitation will increase significantly at the level of 99% using the T test in northern Asia (Figure 5a) and decrease slightly in southern Asia (Figure 5b) after the GHG 1990. This is coherent with the result in Figures 3 and 4. It is notable that the interannual variability of the precipitation in southern Asia with timescales of 2 ~ 3 years will enhance after the GHG 1990 (Figure 5b). It is found that the pre-

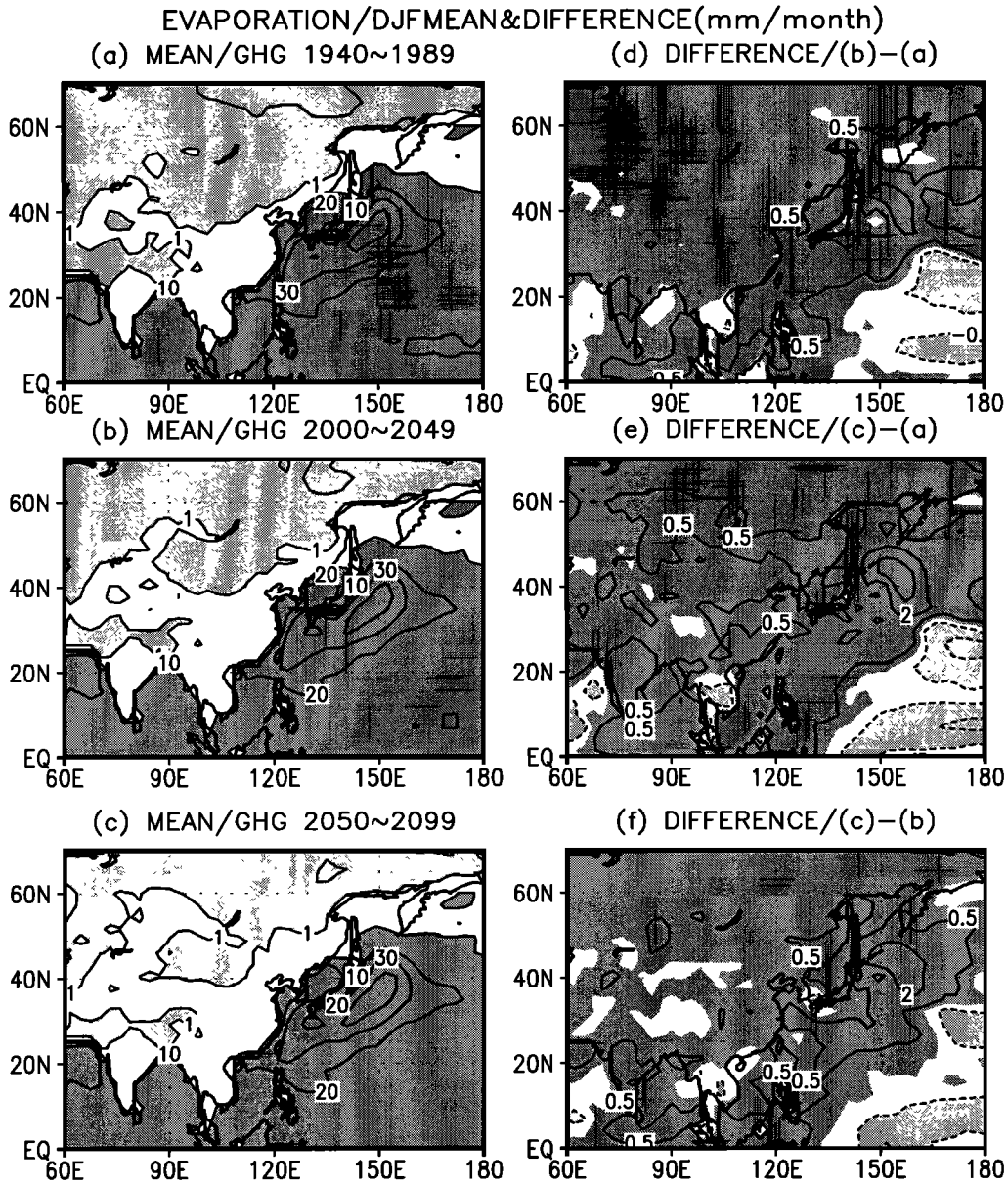

Figure 6. Same as Figure 3 but for the surface evaporation. Contours are at 0, 1, 10, 20, 30, 40 mm/month in Figures 6a-6c, and at −5, −2, −0.5, 0.5, 2, 5 mm/month in Figures 6d-6f. Darker (lighter) shading indicates the regions with values greater (less) than 10 (1) mm/month in Figures 6a-6c, 0.0 (−0.5) mm/month in Figures 6d-6f.

cipitation (snowfall) change is region dependent over the Tibet Plateau, but the average will increase slightly for the whole region of the Tibet Plateau in the global warming scenario (Figure 5c). It is expected that winter precipitation (snow cover) changes in the Tibet Plateau and the Asian continent in the global warming scenario will have a notable feedback on the general circulation in the NH and on the Asian summer monsoon [*Douville and Royer*, 1996].

Evaporation is much larger over the oceans than over the lands (Figures 6a, 6b, and 6c). The impact of the global warming on the evaporation is mainly concentrated in the regions over the Asian continent and from the tropical western Pacific to the northwestern Pacific with enhanced evaporation (Figures 6d, 6e, and 6f). A decreased evaporation is visible over the tropical and subtropical central Pacific (Figures 6d, 6e, and 6f). The distribution patterns of the total precipitation minus the evaporation ($P - E$) are similar for the various periods of the GHG run (Figures 7a, 7b, and 7c). In comparison with the period of the present climate (GHG 1940 ~ 1989), $P - E$ will increase in the high latitudes of the Asian continent, North Pacific, and the tropical and subtropical central Pacific and decrease in the regions from the tropical Indian Ocean to the northwestern Pacific via the tropical western Pacific in the global

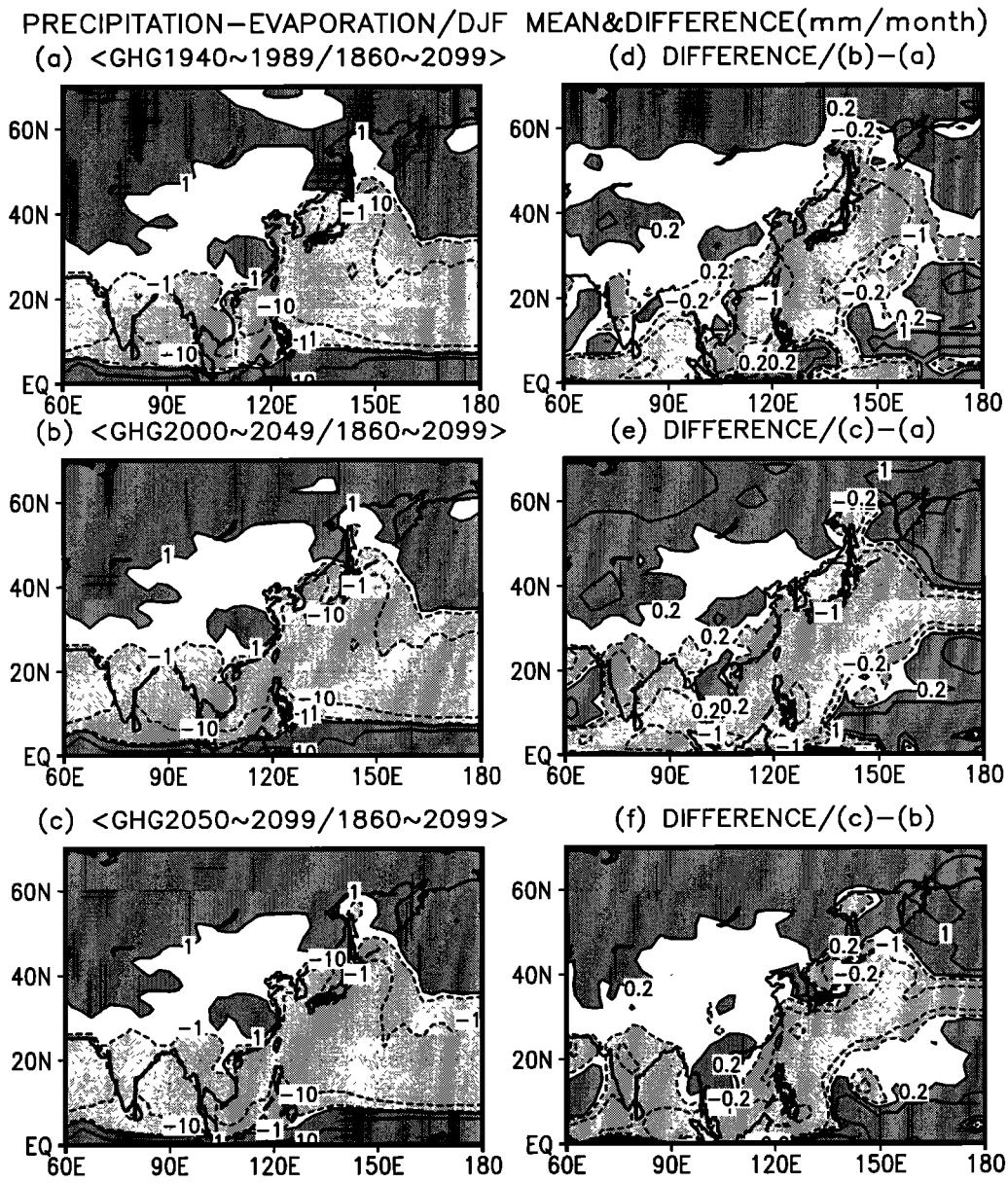

Figure 7. Same as Figure 3 but for the total precipitation minus the surface evaporation. Contours are at 1, 10, 20 mm/month in Figures 7a-7c, at −10, −5, −1, −0.2, 0.2, 1, 5, 10 mm/month in Figures 7d-7f. Darker (lighter) shading indicates the regions with values greater (less) than 10 (1) mm/month in Figures 7a-7c, and 0.2 (−0.2) mm/month in Figures 7d-7f.

warming scenario (Figures 7d, 7e, and 7f). The impacts of the global warming on the evaporation and $P-E$ are more pronounced in the GHG 2000 ~ 2049 than in the GHG 2050 ~ 2099 (Figures 6, 7). Moisture in the soil and low levels of atmosphere will increase (decrease) in the regions with positive (negative) values of $P-E$ in the global warming scenario. This suggests that the global warming will make the climate to be milder in the most parts of Asia, especially in the high latitudes, with enhanced moisture in winter. However, it should be pointed out that the above results are obtained from just one scenario run, and some of the precipitation and evaporation changes may be model dependent, especially in the high latitudes.

4. Mechanism of the AWM Response to Greenhouse Warming

In this section, the mechanism of the AWM response to the greenhouse warming is investigated through analyzing variations near the ground (T2m and SLP) and in the middle and upper troposphere (H300 − H700) in the Asian and western Pacific regions. The distributions of T2m and SLP in the Asian and western Pacific

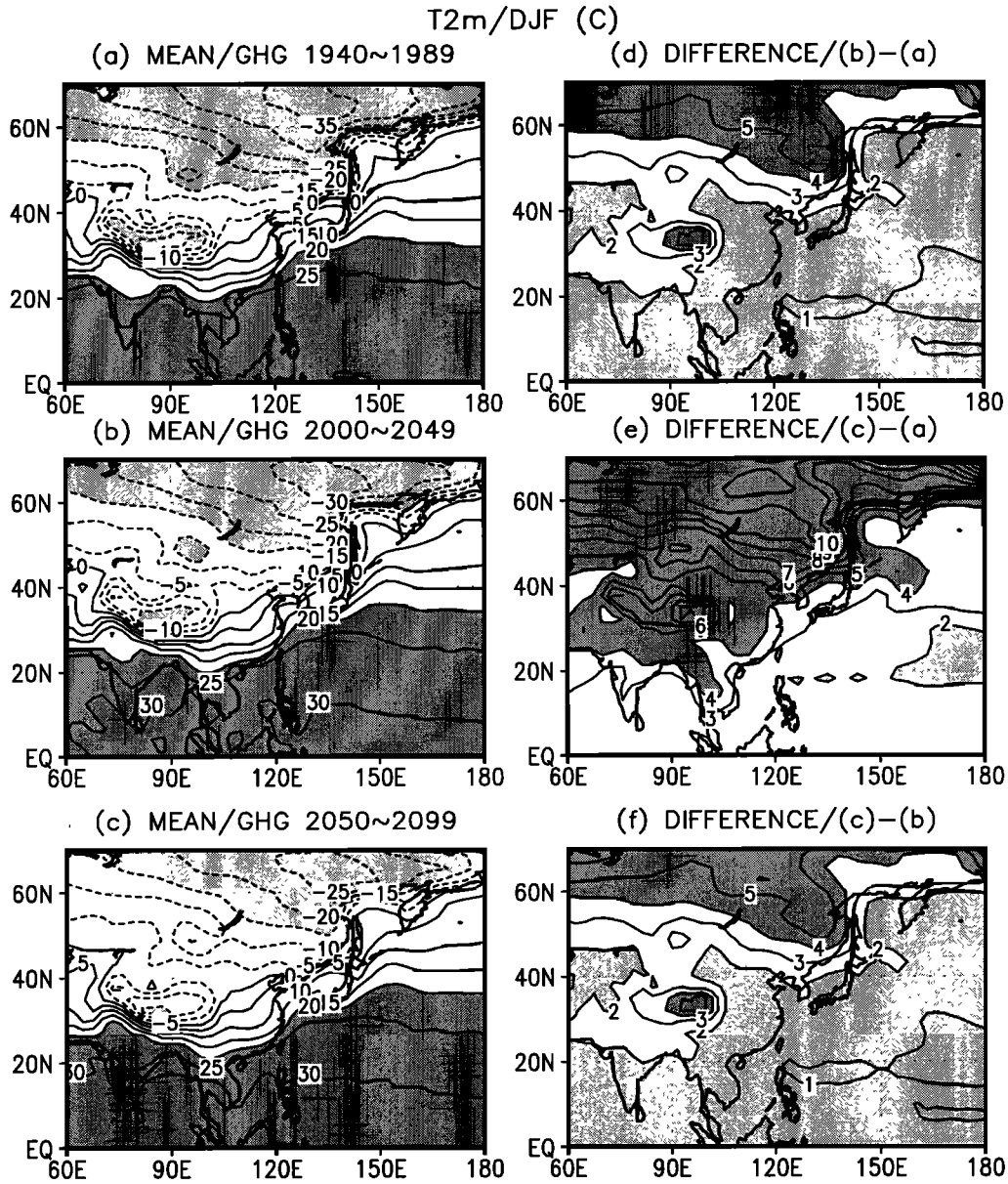

Figure 8. Same as Figure 3 but for the T2m. Contour intervals are 5°C in Figures 8a-8c, and 1°C in Figures 8d-8f. Darker (lighter) shading indicates the regions with values greater (less) than 20 (−15) °C in Figures 8a-8c, and 4 (2) °C in Figures 8d-8f.

regions are directly associated with the AWM, and the thickness distribution (H300 − H700) in high latitudes is related to the variations of the trough and jet stream over east Asia, which are the regulator of cold air in the AWM and energy of the AWM activity [*Ding,* 1991]. The localized Eliassen-Palm flux and its divergence at 300 hPa in the Asian and western Pacific region give an insight of feedback effects of the transient flow on the zonal circulation in various periods of the GHG integration.

4.1. Variations Near the Ground

Figure 8 shows the average of T2m in the (Figure 8a) GHG 1940 ~ 1989, (Figure 8b) GHG 2000 ~ 2049, (Figure 8c) GHG 2050 ~ 2099, and their difference (Figures 8d, 8e, and 8f). In comparison with the mean in the GHG 1940 ~ 1989 (Figure 8a) the temperature will increase over the whole domain in the global warming scenario (Figures 8d, 8e). However, as the temperature increasing is much more manifest over the Asian continent than over the Pacific Ocean (Figures 8d, 8e, and 8f), the temperature contrast between the cold land and the warm ocean in boreal winter will be reduced pronouncely in the global warming scenario, especially in the GHG 2050 ~ 2099 (Figures 8c, 8e, and 8f). The distribution patterns in Figures 8d, 8e, and 8f are coherent with the changes in annual mean surface temperature in the ECHAM4/OPYC3 CGCM with different forcing

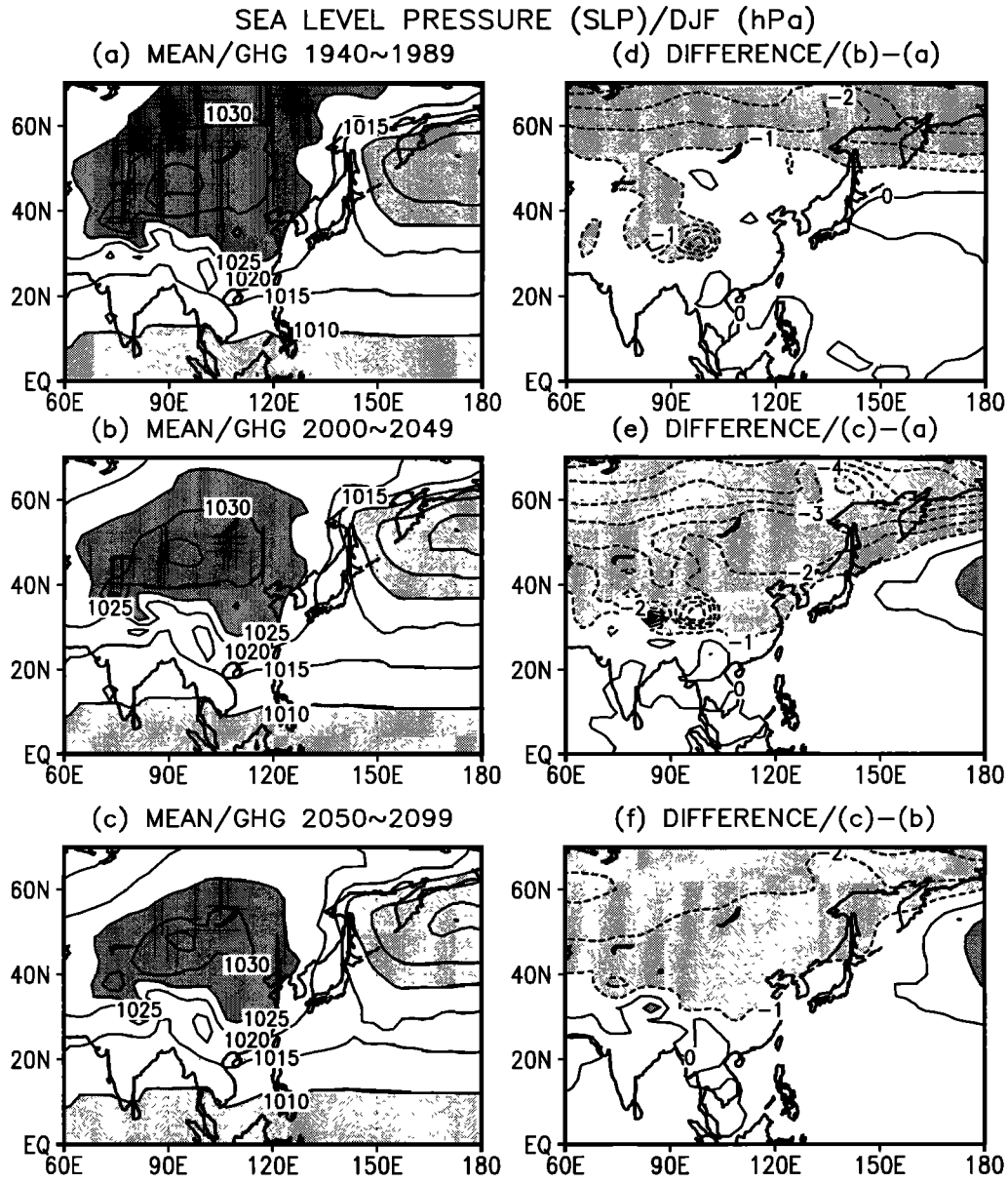

Figure 9. Same as Figure 3 but for SLP. Contour intervals are 5 hPa in Figures 9a-9c, and 1 hPa in Figures 9d-9f. Darker (lighter) shading marks the regions with values greater (less) than 1025 (1010) hPa in Figures 9a-9c, and 1 (−1) hPa in Figures 9d-9f.

scenarios [see *Roeckner et al.*, 1999, Figure 8], which are also typical for the region for the strong warming scenario used.

SLP changes due to the global warming exist over the Asian and western Pacific regions. Comparing the SLP distribution in Figures 9b and 9c with that in Figure 9a, it is indicated that the Siberian high is weakened both for its intensity and range in the period with significant warming (GHG 2000 ~ 2049, GHG 2050 ~ 2099) in contrast with that in the period without significant warming (GHG 1940 ~ 1989). From the difference (Figures 9d, 9e, and 9f) the decrease of SLP is demonstrated over temperate and high latitudes of the Asian continent, and minor increases of SLP is also visible over the North Pacific along about 30°N ~ 50°N, especially in the GHG 2050 ~ 2099 (Figures 9c, 9e, and 9f). This is agreed with *Roeckner et al.* [1999] (see their Figure 14). The similarity of the distribution patterns between the SLP differences (Figures 9d, 9e, and 9f) and the T2m differences (Figures 8d, 8e, and 8f) suggests the coherent and coupling relation between SLP and T2m variations over the Asian and western Pacific regions. The change between the SLP in the temperate and high latitudes of the Asian continent and over the North Pacific is significant (see Figure 10).

Figure 10 shows the temporal variations of SLP and T2m gradients along latitudes between the Asian continent and the western Pacific. The longitudinal gradient

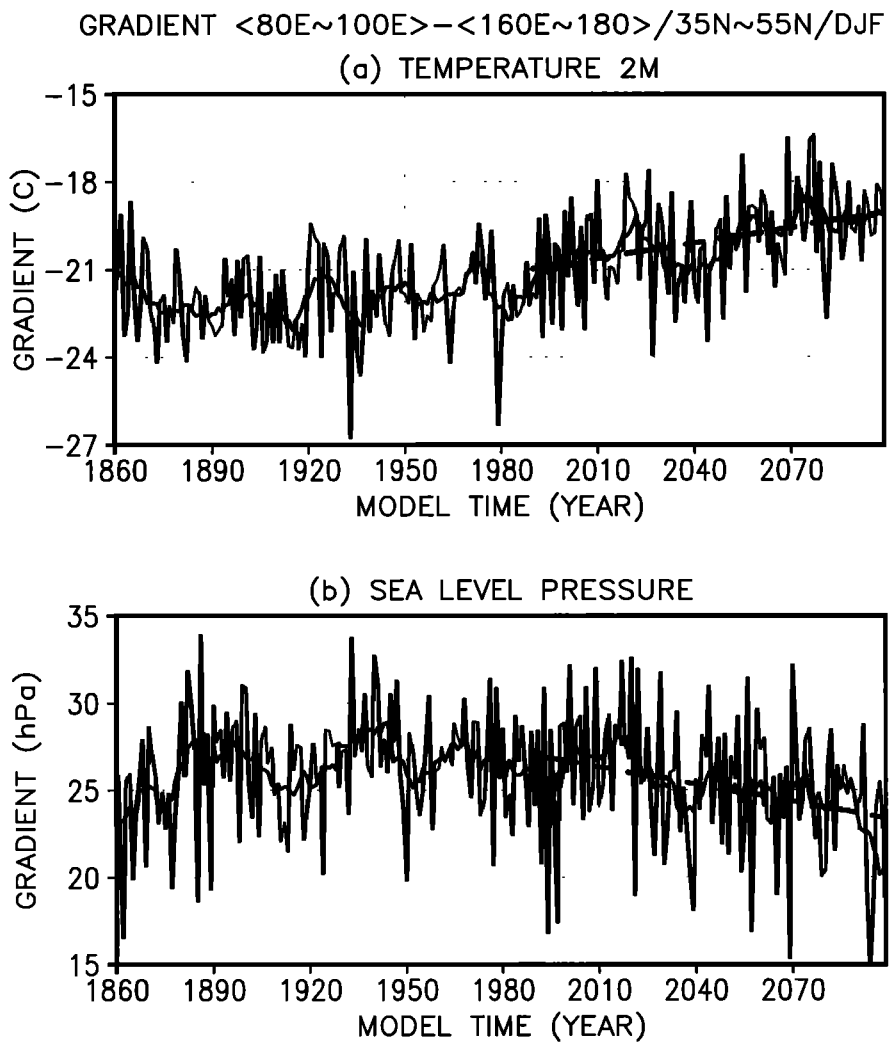

Figure 10. Same as Figure 2 but for the variations of the gradient of (a) T2m and (b) SLP between the mean of 80°E ~ 100°E and the mean of 160°E ~ 180° averaged in the latitudes of 35°N ~ 55°N. The linear trends are 0.018°C per year and −0.033 hPa per year for the period of the GHG 1990 ~ 2099 in Figures 10a and 10b, respectively. The linear trends (long-dashed lines) during the GHG 1990 ~ 2099 in Figures 10a and 10b are different from zero at the significance level of 99% using the T test. The units are (a) °C and (b) hPa.

is defined as the difference between the mean of 80°E ~ 100°E and the mean of 160°E ~ 180° averaged in the latitudes of 35°N ~ 55°N. The region of (80°E ~ 100°E, 35°N ~ 55°N) represents the variations of SLP and T2m associated with the Siberian high, and the region of (160°E ~ 180°, 35°N ~ 55°N) reflects the variations of SLP and T2m over the North Pacific. Interannual and interdecadal variations are clearly demonstrated in Figure 10. Linear trends of decreasing SLP and T2m gradients are pronounced after the year 1990 in the GHG run. They are different from zero at the significance level of 99% using the T test. Therefore the SLP and T2m contrasts between the Asian continent and the Pacific Ocean become significantly smaller in the global warming scenario.

4.2. Variations in the Middle and Upper Troposphere

Intensities and locations of the jet stream and the trough over east Asia in the middle and upper troposphere are closely related with the activity and strength of the AWM. Figure 11 shows the average of H300−H700 in the (Figure 11a) GHG 1940 ~ 1989, (Figure 11b) GHG 2000 ~ 2049, (Figure 11c) GHG 2050 ~ 2099, and their difference (Figures 11d, 11e, 11f). In the global warming scenario the central value of the thickness is increased from 5700 geopotential meters (gpm) in Figure 11a to 5800 gpm in Figures 11b and 11c. In the different fields (Figures 11d, 11e, and 11f), larger values are in the Eurasian continent with the central values exceeded 60, 125, and 75 gpm in Figures 11d, 11e,

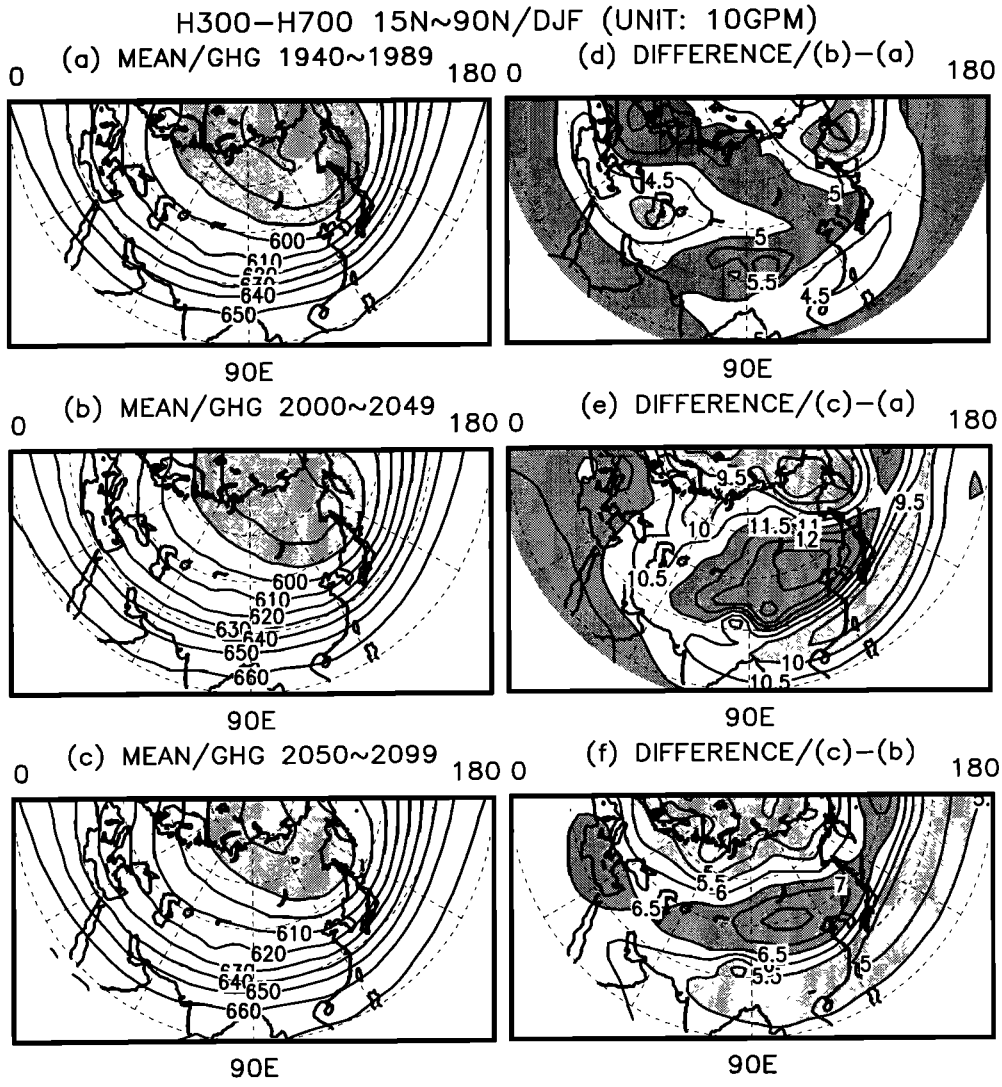

Figure 11. Same as Figure 3 but for H300–H700 over the region (15°N ~ 90°N, 0° ~ 180°). Contour intervals are 100 gpm in Figures 11a-11c, and 5 gpm in Figures 11d-11f. Shading marks the regions with values less than 5900 gpm in Figures 11a-11c. Darker (lighter) shading marks the regions with values greater (less) than 50 (40) gpm in Figure 11d, 110 (100) gpm in Figure 11e, and 65 (55) gpm in Figure 11f.

and 11f, respectively, and smaller values by the northern and southern sides. The change resulted from the global warming in the GHG 2050 ~ 2099 is more evident than in the GHG 2000 ~ 2049 (Figures 11d, 11e, and 11f). This kind of distribution with larger values by the western side and relatively smaller values by its eastern side of the east Asian trough (located in 120°E ~ 150°E) reflects the eastward shift of the east Asian trough in the global warming scenario. Figures 11d, 11e, and 11f also demonstrate the weakening and northward shift of the maximum gradient between the south and north sides of the jet stream and trough over east Asia, as larger values of the thickness changes are in the central part of the Eurasian continent and smaller values by its southeastern side along 20°N ~ 30°N. Therefore it is concluded that the jet stream and trough over east Asia will shift eastward and northward and weaken as well in the global warming scenario. The change of the average of H300 – H700 associated with the jet stream and trough over east Asia in Figure 11 is significant (see Figure 12).

Figure 12 shows temporal variations of the gradients of H300–H700 between the western (90°E ~ 120°E) and the eastern (140°E ~ 170°E) sides of the east Asian trough averaged along 40°N ~ 60°N (Figure 12a) and between the southern (20°N ~ 30°N) and northern (35°N ~ 50°N) sides of the east Asian trough averaged along 100°E ~ 130°E (Figure 12b). Beside interannual and interdecadal variations, linear trends are pronounced, which are different from zero at the significance levels of 95% and 99% in Figures 12a and 12b using the T test, respectively. The increasing trend of the

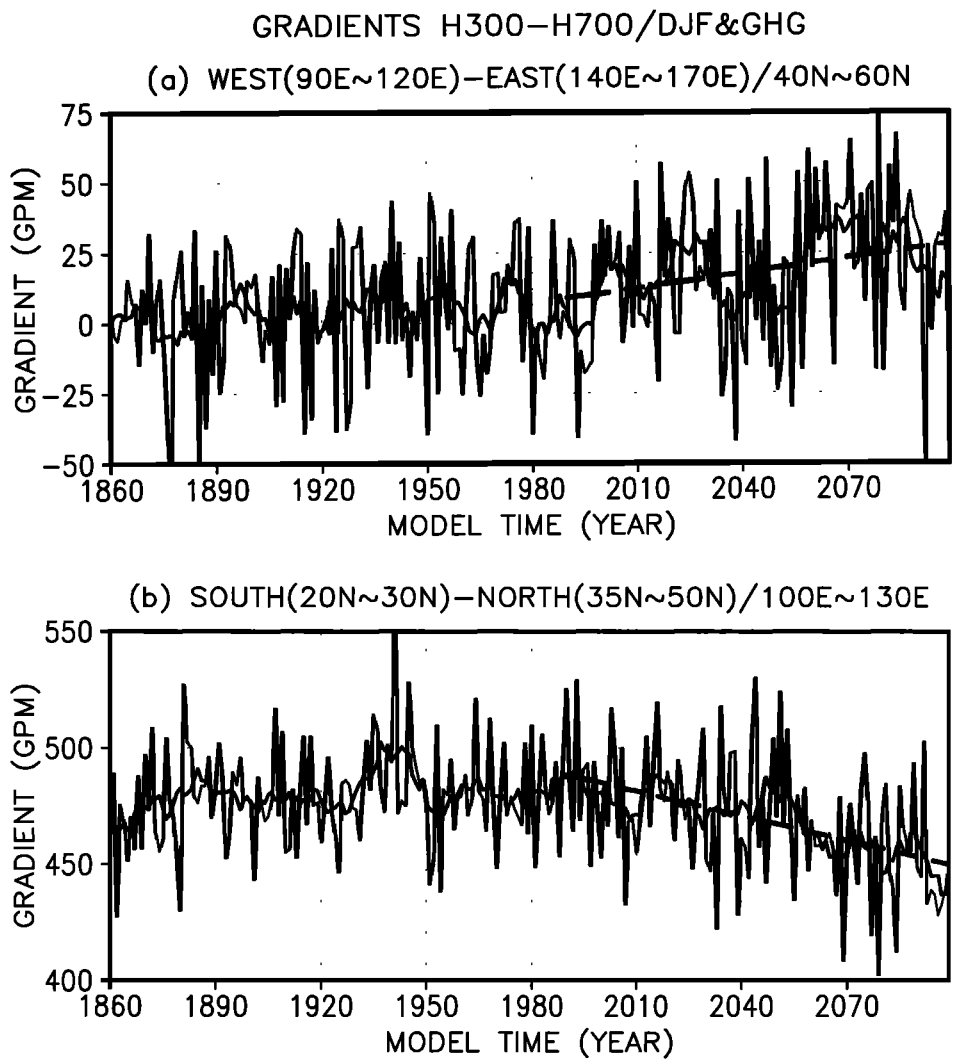

Figure 12. Same as Figure 2 but for the variations of the gradients of H300−H700 (a) between the western (90°E ~ 120°E) and eastern (140°E ~ 170°E) sides of the east Asian trough averaged along 40°N ~ 60°N, and (b) between the southern (20°N ~ 30°N) and northern (35°N ~ 50°N) sides of the east Asian trough averaged along 100°E ~ 130°E. The long-dashed lines are the linear trends of the gradients during the GHG 1990 ~ 2099, which are different from zero at the significance levels of 95% and 99% in Figures 12a and 12b using the T test, respectively. The units are gpm. The linear trends are 0.18 and −0.35 gpm per year for the period of the GHG 1990 ~ 2099 in Figures 12a and 12b, respectively.

gradient in Figure 12a mainly reflects the eastward shift of the east Asian trough, and the decreasing trend in Figure 12b demonstrates the weakening and northward shift of the east Asian trough in the global warming scenario. The weakening and eastward and northward shifts of the east Asian trough will make the cold waves and cold air in the AWM to be less powerful in the Asian region. This corresponds to the weakening trend of the AWM in the global warming scenario.

4.3. Transient Activity

The AWM has a mean and a transient component of which the transient part has a more dramatic impact on the daily weather. The integral effect of the transient activities associated with the cold fronts and cold waves over east Asia and its feedback play an important role in the AWM variations. The large values of zonal component of the two-dimensional (latitudinal and longitudinal) localized Eliassen-Palm flux (E) and its divergence ($\nabla \bullet E$) for various periods in the GHG run at 300 hPa in the Asian and western Pacific regions are mainly concentrated in the North Pacific associated with the jet stream and storm tracks (Figures 13a, 13b, 13c, and 13d). There exist systematic and pronounced changes of the localized Eliassen-Palm flux and its divergence due to the global warming in the Asian and western Pacific regions (Figures 13e, 13f, and 13g). A coherent signal from the global warming is an anomalous convergence of the localized Eliassen-Palm flux in

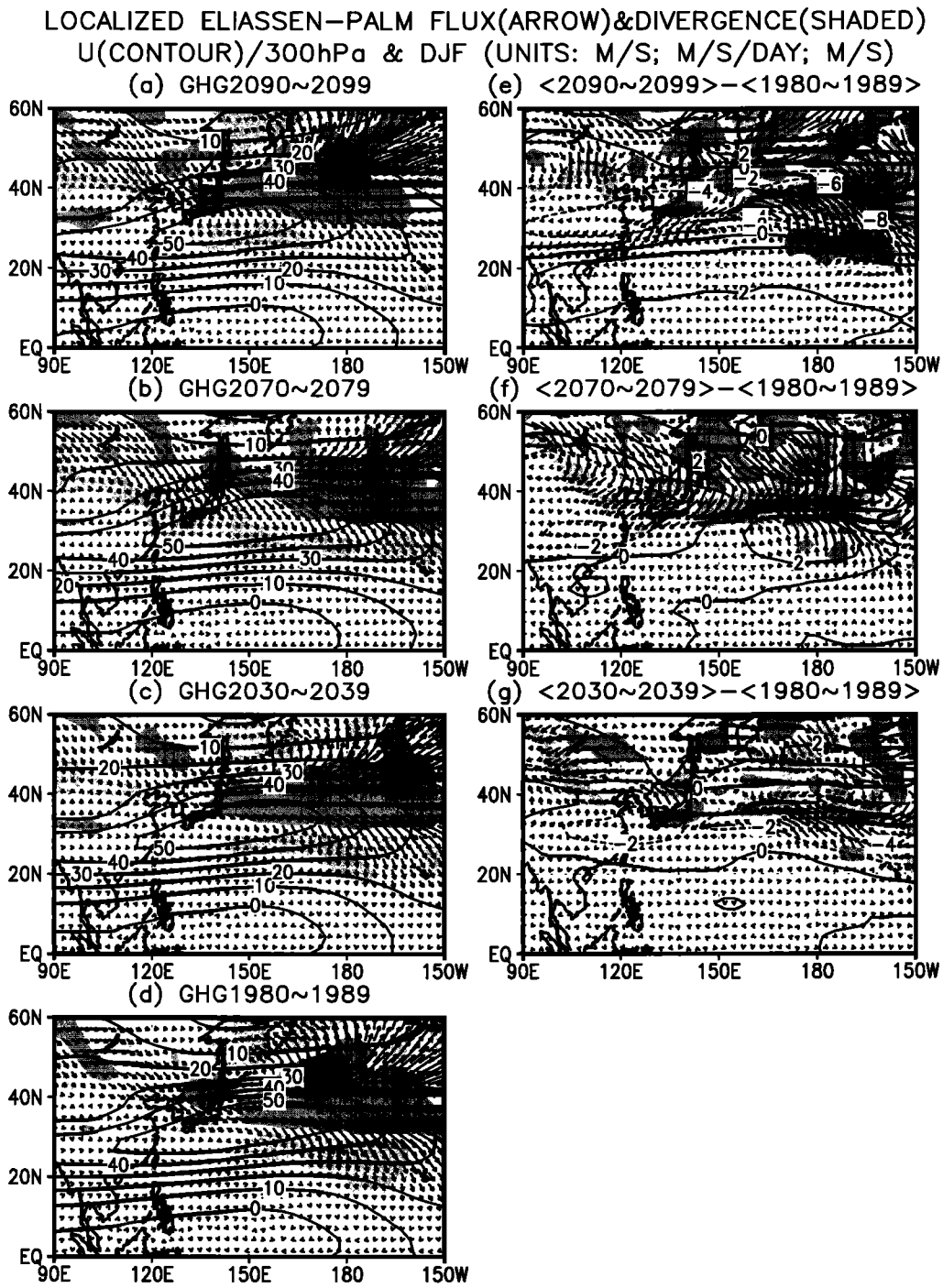

Figure 13. Localized Eliassen-Palm flux (arrow), its divergence (shaded), and u component of the wind field (contour) at 300 hPa in winter for the decadal averages in the periods of (a) the GHG 2090 ~ 2099, (b) the GHG 2070 ~ 2079, (c) the GHG 2030 ~ 2039, and (d) the GHG 1980 ~ 1989, and the difference: (e) Figures 13a minus 13d, (f) Figures 13b minus 13d, (g) Figures 13c minus 13d. Darker (lighter) shading marks the regions with values greater (less) than 0.5 (−0.5) m/s/d for the divergence of the localized Eliassen-Palm flux. The contour intervals are 10 m/s in Figures 13a-13d, and 2 m/s in Figures 13e-13g. The dashed lines represent the negative values in Figures 13e-13g.

the Pacific Ocean along 25°N ~ 40°N, which is in favor of decelerating westerlies in the core of the jet stream (Figures 13e, 13f, and 13g). Anomalous divergence is also evident in the northwestern Pacific along the coast, but the area of action changes from one to another period (Figures 13e, 13f, and 13g), which is in favor of accelerating westerlies. However the deceleration in the Pacific Ocean along 25°N ~ 40°N is larger than the acceleration in the latitudes farther north. The changes of the localized Eliassen-Palm flux and its convergence

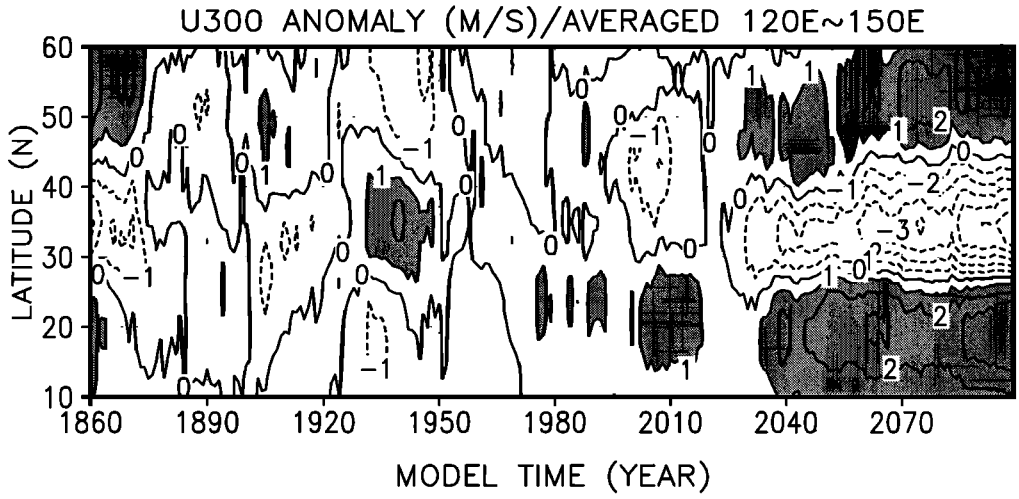

Figure 14. Time-latitude diagram of the anomalies of the zonal component of the wind field at 300 hPa averaged $120^oE \sim 150^oE$. The anomalies are calculated relative to the mean of 1860 ~ 1979. The dashed lines represent the negative values. The shading marks the regions with the values larger than 1 m/s. The contour intervals are 1 m/s.

in the Pacific Ocean along 25°N ~ 40°N are consistent with the changes of the thickness gradients in the global warming scenario shown in Figures 11d, 11e, and 11f.

Figure 14 shows the temporal evolution of the anomalies of the zonal component of the wind field at 300 hPa along 10°N ~ 60°N averaged 120°E ~ 150°E. The systematic weakening and northward shift of the jet stream over east Asia after the GHG 2020 are clearly demonstrated in Figure 14. The northward shift of the jet stream at 300 hPa over the North Pacific reflects the poleward withdrawing of the cold air in high latitudes, which associated with the weakening of the AWM in the global warming scenario. So, in the global warming scenario, the feedback of the transient activity forces the jet stream over the North Pacific to be shifted to the higher latitudes. The northward shift of the jet stream forced by the transient activities over the North Pacific agrees with the poleward shift of the east Asian trough (Figures 11, 12), and also cohered with the total precipitation changes over the Asian and western Pacific regions (Figures 3, 4).

5. Summary and Discussion

The Asian winter monsoon (AWM) response to the global warming was investigated through a long-term integration of the transient greenhouse warming with the ECHAM4/OPYC3 CGCM. The physics of the response was studied through analyses of the impact of the global warming on the variations of the ocean and land contrast near the ground (T2m and SLP) in the Asian and western Pacific regions and the east Asian trough and jet stream in the middle and upper troposphere (H300 − H700). Forcing of transient eddy activity on the zonal circulation over the Asian and western Pacific regions was also analyzed.

It is found that in the global warming scenario the winter northeasterlies along the Pacific coast of the Eurasian continent weaken systematically and significantly, and the intensity of the AWM reduces evidently, but the AWM variances on the interannual and interdecadal scales are not affected much by the global warming. The corresponding changes of precipitation and evaporation over some regions of Asia and the western Pacific region are pronounced. It is suggested that the global warming makes the climate to be milder over the most part of Asia (especially in the high latitudes) with enhanced moisture in winter.

In the global warming scenario the contrasts of the sea level pressure and near-surface temperature between the Asian continent and the Pacific Ocean become significantly smaller, northward and eastward shifts and weakening of the east Asian trough and jet stream in the middle and upper troposphere are found. As a consequence, the cold air in the AWM originating from the east Asian trough and high latitudes is less powerful. The northward shifts of the jet stream in the middle and upper troposphere over the North Pacific in the global warming scenario can be partly attributed to the feedback of the transient activity.

Significant impacts of the global warming on the AWM have been demonstrated by the above analyses in the long-term integration with the ECHAM4/OPYC3 CGCM. The weakened AWM in the global warming scenario is cohered with the weakened Hadley cell over the Asian and western Pacific regions (Figure 15), which will influence the interactions between two hemispheres and between low and high latitudes. The weakened Hadley cell may be mainly the result of the reducing temperature gradients between low and high latitudes in the troposphere in the global warming scenario, as the temperature increases are more pronounced in the

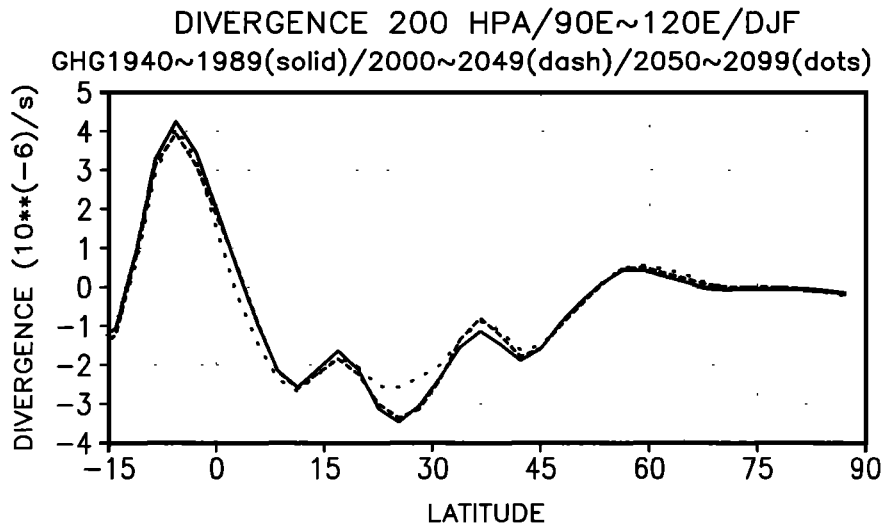

Figure 15. Divergences at 200 hPa along $15^oS \sim 90^oN$ averaged in $90^oE \sim 120^oE$ and in the periods of the GHG 1940 $\sim$ 1989 (solid), GHG 2000 $\sim$ 2049 (dashed), and GHG 2050 $\sim$ 2099 (dotted). The units are 10^{-6} s^{-1}.

high latitudes than in the low latitudes, as shown in Figures 8 and 11. The changed wind field, precipitation, and evaporation in the AWM region in the global warming scenario will influence the energy and hydrological cycles inside and outside the region. For example, the weakened AWM is coherent with suppressed convection activity over the warm pool region in the western Pacific (Figure 3). It is expected that the feedback of the convection variation over the warm pool region will have some impact on the climate and general circulation in the NH [*Hu and Nitta*, 1997; *Nitta*, 1987]. The association of the changed AWM with the circulation and climate in the NH or even in the globe is out of the scope of the present paper.

The feedback of the transient activity on the zonal circulation has been demonstrated in this work, but the transient activity associated with the daily variability of the AWM is largely organized and modulated by the stationary and quasi-stationary waves. This is a two-way interaction. In this work, only the feedback of the transient activity on the waves was analyzed through investigating the localized Eliassen-Palm flux and its divergence for various periods in the GHG run. It is still an open question of the impact of changed stationary and quasi-stationary waves in the global warming scenario on the transient component of the AWM.

There are some significant limitations of the results obtained in this study. One is from the coarse resolution (T42) of the model used in this work. Recent investigations [e. g., *Stendel and Roeckner*, 1998] have indicated that a model with a higher resolution can give more realistic climate simulations than the model with a lower resolution, especially for regional climate changes. The quantitative results of regional climate changes in a global GCM simulation sometimes is sensitive to the model resolution. A similar integration with a higher horizontal and vertical resolution model should be done as the computing power is available. Comparison of the present results with the results from various resolution models and from different-type models is also necessary as one topic of future researches. Another limitation of the present results is using one official IPCC scenario (IS92a). Evidently, it is not enough for arriving at realistic conclusions on the next century climate change. More scenarios are needed for an ensemble run that may produce more meaningful results, especially for regional climate change estimates. Therefore to predict the next century climate change with higher accuracy, it is necessary to make some ensemble runs with different models and various scenarios.

Acknowledgments. The authors thank the editor R. Avissar and two anonymous reviewers for their suggestions and comments to significantly improve the manuscript. The authors are indebted to H.-S. Bauer, Z. Liu, M. Esch, R. Budich, and other colleagues at Max-Planck-Institut für Meteorologie, Hamburg, Germany, for their help with data processing and graphics programming. Special thanks are due to M. Christoph for his kind supply of the bandpass data and helpful discussion. The first author (Hu) is grateful to E. Roeckner, L. D. Gates, and J. M. Oberhuber for their encouragement. The figures in this article were prepared using the graphics software GrADS, developed by Brian Doty of COLA/IGES.

References

Bacher, A., J. M. Oberhuber, and E. Roeckner, ENSO dynamics and seasonal cycle in the tropical Pacific as simulated by the ECHAM4/OPYC3 coupled general circulation model, *Clim. Dyn., 14*, 431-450, 1998.

Bengtsson, L., The climate response to the changing greenhouse gas concentration in the atmosphere, *NATO ASI Ser.*, vol. I44, *Decadal Climate Variability, Dynamics and Predictability*, edited by D. L. T. Anderson and J. Willebrand, pp. 293-332, Springer-Verlag, New York, 1996.

Bengtsson, L., A numerical simulation of anthropogenic climate change, *Ambio, 26*, 58-65, 1997.

Chang, C.-P., J. Erickson, and K.-M., Lau, Northeasterly cold surges and near-equatorial disturbances over the winter-MONEX area during December 1974, part I, Synoptic aspects, *Mon. Weather Rev., 107*, 812-829, 1979.

Chen, C.-T., and E. Roeckner, Validation of the earth radiation budget as simulated by the Max Planck Institute for Meteorology general circulation model ECHAM4 using satellite observations of the Earth Radiation Budget Experiment, *J. Geophys. Res., 101*, 4269-4287, 1996.

Chen, L., Q. Zhu, and H. Luo, *East Asian Monsoon*, (in Chinese), 362 pp., China Meteorol. Press, Beijing, 1991.

Chen, W., and Hans-F. Graf, The interannual variability of East Asian winter monsoon and its relation to global circulation, *Adv. Atmos. Sci.*, in press, 1999.

Compo, G. P., G. N. Kiladis, and P. J. Webster, The horizontal and vertical structure of east Asian winter monsoon pressure surges, *Q. J. R. Meteorol. Soc., 125*, 29-54, 1999.

Ding, Y., *Advanced Synoptics*, (in Chinese), 792 pp., China Meteorol. Press, Beijing, 1991.

Douville, H., and J.-F. Royer, Sensitivity of the Asian summer monsoon to an anomalous Eurasian snow cover within the Meteo-France GCM, *Clim. Dyn., 12*, 4449-466, 1996.

Hu, Z.-Z., and T. Nitta, Seasonality of the interaction between convection over the western Pacific and general circulation in the Northern Hemisphere, *Adv. Atmos. Sci., 14*, 541-553, 1997.

Hu, Z.-Z., L. Bengtsson, E. Roeckner, M. Christoph, A. Bacher, and J. M. Oberhuber, Impact of global warming on the interannual and interdecadal climate modes in a coupled GCM, *Clim. Dyn.*, in press, 1999.

Hulme, M., Z. C. Zhao, and T. Jiang, Recent and future climate change in East Asia, *Int. J. Climatol., 14*, 637-658, 1994.

Intergovernmental Panel on Climate Change (IPCC), *Climate Change 1992, The Supplementary Report to the IPCC Scientific Assessment*, edited by J. T. Houghton, B. A. Callander, and S. K. V. Varney, 198 pp., Cambridge Univ. Press, New York, 1992.

Ji, L., S. Sun, K. Arpe, and L. Bengtsson, Model study on the interannual variability of Asian winter monsoon and its influence, *Adv. Atmos. Sci., 14*, 1-22, 1997.

Lau, K.-M., East Asian summer monsoon rainfall variability and climate teleconnection, *J. Meteorol. Soc. Jpn., 70*, 211-241, 1992.

Li, C., Y. Chen, and C. Yuan, An important causative factor of El Niño event-frequent activities of strong cold waves in East Asia, (in Chinese), *Sci. Atmos. Sin., 12*, 125-131, 1988.

Nitta, T., Convective activities in the tropical western Pacific and their impact on the Northern Hemisphere summer circulation, *J. Meteorol. Soc. Jpn., 65*, 373-390, 1987.

Nitta, T., and Z.-Z. Hu, Summer climate variability in China and its association with 500 hPa height and tropical convection, *J. Meteorol. Soc. Jpn., 74*, 425-445, 1996.

Oberhuber, J. M., The OPYC ocean general circulation model, *Dtsch. KlimaRechZent. (DKRZ) Tech. Rep., 7*, 1-130, 1993a.

Oberhuber, J. M., Simulation of the Atlantic circulation with a coupled sea-ice-mixed layer-isopycnal general circulation model, part I, Model description, *J. Phys. Oceanogr., 22*, 808-829, 1993b.

Roeckner, E., K. Arpe, L. Bengtsson, M. Christoph, M. Claussen, L. Dümenil, M. Esch, M. Giorgetta, U. Schlese, and U. Schulzweida, The atmospheric general circulation model ECHAM-4: Model description and simulation of present-day climate, *Max-Planck-Inst. Meteorol. Rep., 218*, 1-90, 1996a.

Roeckner, E., J. M. Oberhuber, A. Bacher, M. Christoph, and I. Kirchner, ENSO Variability and atmospheric response in a global coupled atmosphere-ocean GCM, *Clim. Dyn., 12*, 737-754, 1996b.

Roeckner, E., L. Bengtsson, J. Feichter, L. Lelieveld, and H. Rodhe, Transient climate change simulations with a coupled atmosphere-ocean GCM including the tropospheric sulfur cycle, *J. Clim., 12*, 3004-3032, 1999.

Stendel, M., and E. Roeckner, Impact of horizontal resolution on simulated climate statistics in ECHAM 4, *Max-Planck-Inst. Meteorol. Rep., 253*, 1-57, 1998.

Sun, B., and S. Sun, The analysis on the features of the atmospheric circulation in preceding winter for the summer drought and flooding in the Yangtze and Huaihe River Valley, *Adv. Atmos. Sci., 11*, 79-90, 1994.

Trenberth, K. E., An assessment of the impact of transient eddies on the zonal flow during a blocking episode using localized localized Eliassen-Palm flux diagnostics, *J. Atmos. Sci., 43*, 2070-2087, 1986.

Wang, S. W., and D. Z. Ye, Analysis of the global warming during the last one hundred years, in *Climate Variability*, edited by Ye et al., pp. 23-32, China Meteorol. Press, Beijing, 1993.

World Climate Research Programme (WCRP), *CLIVAR Initial Implementation Plan, WCRP 103, WMO/TD 869, ICPO 14*, 314 pp., World Meteorol. Organ., Geneva, 1998.

Yasunari, T., The monsoon year: A new concept of the climatic year in the tropics, *Bull. Am. Meteorol. Soc., 72*, 1331-1338, 1991.

K. Arpe, L. Bengtsson, and Z.-Z. Hu, Max-Planck-Institut für Meteorologie, Hamburg, Germany. (e-mail: arpe@dkrz.de; bengtsson@dkrz.de; hu@dkrz.de)

(Received March 29, 1999; revised July 28, 1999; accepted September 21, 1999.)